GEOPHYSICS, VOL. 83, NO. 3 (MAY-JUNE 2018); P. WC71–WC81, 7 FIGS., 2 TABLES.
10.1190/GEO2017-0549.1

Effects of ellipsoidal heterogeneities on wave propagation in partially saturated double-porosity rocks

Weitao Sun[1], Fansheng Xiong[1], Jing Ba[2], and José M. Carcione[3]

ABSTRACT

Reservoir rocks are heterogeneous porous media saturated with multiphase fluids, in which strong wave dissipation and velocity dispersion are closely associated with fabric heterogeneities and patchy saturation at different scales. The irregular solid inclusions and fluid patches are ubiquitous in nature, whereas the impact of geometry on wave dissipation is still not well-understood. We have investigated the dependence of wave attenuation and velocity on patch geometry. The governing equations for wave propagation in a porous medium, containing fluid/solid heterogeneities of ellipsoidal triple-layer patches, are derived from the Lagrange equations on the basis of the potential and kinetic energies. Harmonic functions describe the wave-induced local fluid flow of an ellipsoidal patch. The effects of the aspect ratio on wave velocity are illustrated with numerical examples and comparisons with laboratory measurements. The results indicate that the P-wave velocity dispersion and attenuation depend on the aspect ratio of the ellipsoidal heterogeneities, especially in the intermediate frequency range. In the case of Fort Union sandstone, the P-wave velocity increases toward an upper bound as the aspect ratio decreases. The example of a North Sea sandstone clearly indicates that introducing ellipsoidal heterogeneities gives a better description of laboratory data than that based on spherical patches. The unexpected high-velocity values previously reported and ascribed to sample heterogeneities are explained by varying the aspect ratio of the inclusions (or patches).

INTRODUCTION

The seismic exploration method is a nondestructive technique to obtain information about the subsurface. Indeed, the P-wave velocity is an effective property of lithology and fluid content (Gregory, 1976). Wave-induced local fluid flow (LFF) (mesoscopic loss) has been recognized as one of the main causes of wave dispersion and attenuation (Müller et al., 2008; Ba et al., 2011, 2016), which is greatly affected by solid-fluid heterogeneities, composed of different types of pore structures, mineral grains, cements, and immiscible fluid patches.

Rocks containing pores and cracks can be approximated with a double-porosity system. The double-porosity continuum model was first introduced by Barenblatt et al. (1960) to study fluid flow between pores and cracks. Aifantis (1977, 1979, 1980), Wilson and Aifantis (1982), and Khaled et al. (1984) developed a framework of multi-porous (or double-porosity) models based on the conservation equations of mass, momentum, and energy. A linear poroelastic constitutive model for dual-porosity media was proposed by Elsworth and Bai (1992) based on the equations of mass conservation. Berryman and Wang (1995, 2000) derived the wave-propagation equations of a double-porosity medium with a host pore system and embedded fractures.

The effects of partial saturation on wave velocities have been widely studied (White, 1975; White et al., 1975; Dutta and Odé, 1979a, 1979b; Dutta and Seriff, 1979; Knight and Nolen-Hoeksema, 1990; Mavko and Mukerji, 1998; Johnson, 2001; Müller and Gurevich, 2004; Pride et al., 2004; Müller et al., 2008; Ba et al., 2011; Sun et al., 2016; Sharma, 2017; Zheng et al., 2017). Experimental observations were reported in the sonic and ultrasonic frequency bands (Wyllie et al., 1956, 1958; Gregory, 1976; Murphy, 1984; Bacri and Salin, 1986; Cadoret et al., 1995, 1998). More

Manuscript received by the Editor 17 August 2017; revised manuscript received 12 February 2018; published ahead of production 23 February 2018; published online 7 May 2018.
[1]Tsinghua University, Zhou Pei-Yuan Center for Applied Mathematics, Beijing, China.
[2]Hohai University, School of Earth Sciences and Engineering, Nanjing, China. E-mail: jba@hhu.edu.cn.
[3]Hohai University, School of Earth Sciences and Engineering, Nanjing, China and Istituto Nazionale di Oceanografia e di Geofisica Sperimentale (OGS), Trieste, Italy.

recently, fluid patch distributions were directly observed in partially saturated rocks using injection experiments and computer tomography (CT) imaging techniques (Lebedev et al., 2009; Lopes and Lebedev, 2012). It is clear that wave velocity dispersion and attenuation are dependent on patch size and spatial distribution (Helle et al., 2003; Toms et al., 2006; Sun et al., 2015). It has been concluded that the wave-induced LFF due to mesoscopic heterogeneities is the main mechanism responsible for energy dissipation in partially saturated rocks (Johnson, 2001; Müller and Gurevich, 2004; Berryman and Pride, 2005; Toms et al., 2006). However, the mechanism by which arbitrary-shaped heterogeneities govern wave dispersion/attenuation still needs further investigations.

Several models were developed to analyze the effects of patchy saturation, theoretically or computationally, for a single-porosity medium saturated with a mixture of immiscible fluids (White, 1975; Dutta and Odé, 1979a, 1979b; Johnson, 2001; Pride et al., 2004; Quintal et al., 2011; Ba et al., 2017) and a double-porosity media saturated with a single fluid (Berryman and Wang, 2000; Pride et al., 2004; Rubino and Holliger, 2012). The effects of randomly distributed fluid patches were studied by Toms et al. (2007). A triple-layer patchy (TLP) model has been proposed for a double-porosity media saturated with two immiscible fluids, which is shown in Figure 1b (Sun et al., 2016). Even though researchers have made many attempts to explain the observed velocity-saturation relationships, the formation and evolution of fluid patches in real rocks are still poorly understood. Recent experiments show that the characteristic patch size may depend on the saturation and injection rate (Toms-Stewart et al., 2009; Lopes et al., 2014). A method has been proposed to model the distinct relationship between the patch size and injection rate (Liu et al., 2016).

The main objective of this work is to derive an ellipsoidal TLP (ETLP) model to incorporate the geometric effects of ellipsoidal solid inclusions and fluid patches in wave propagation (Figure 1c). This model is more general than those based on spherical patches, especially for deeply buried tight rocks containing flat pore spaces and penny-shaped cracks. The new model differs from the previous TLP model in three respects: (1) the solid and fluid inhomogeneities are analyzed in terms of concentric ellipsoids, which incorporate the effects of the aspect ratio (see Figure 2), (2) the ellipsoidal patches are randomly distributed in space (isotropy), and (3) the size and aspect ratio of the ellipsoids are random. Here, the volume fraction of the inner fluid pocket is constant.

As shown in Figure 1c, the ellipsoids are randomly distributed in space. The aspect ratio can be larger or smaller than unity. Although the semiaxes are assumed to be aligned with the Cartesian coordi-

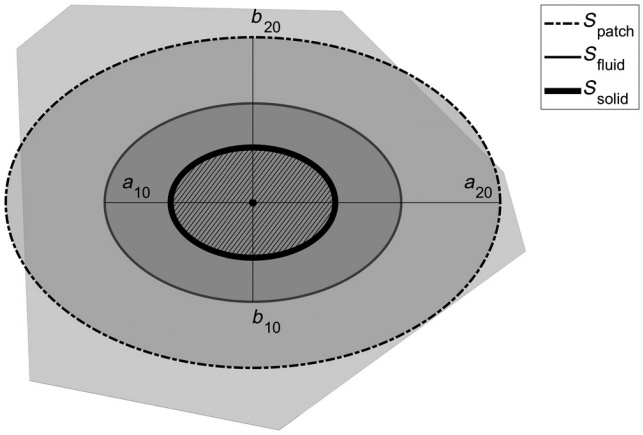

Figure 2. A 2D diagram of an ETLP. The irregular volume containing the solid and fluid inhomogeneities is represented by the equivalent concentric ellipsoidal shells. Two porous components are separated by the interface S_{solid}. The two immiscible fluids are separated by the interface S_{fluid} with radii (a_{10}, b_{10}, c_{10}). The overall ellipsoidal patch has the radii (a_{20}, b_{20}, c_{20}).

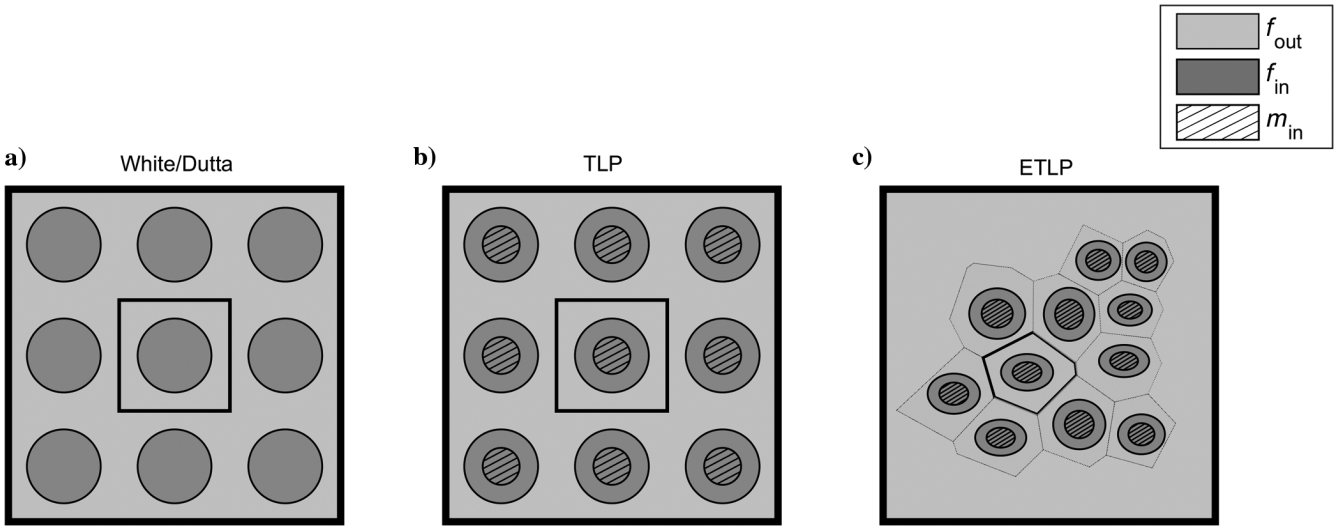

Figure 1. Diagrams of mesoscopic patchy models. (a) White/Dutta model: A porous skeleton saturated with water (the host background) contains spherical gas pockets (dark shaded patches). (b) TLP model: A porous skeleton saturated with an immiscible fluid f_{out} (host fluid) contains uniform spherical heterogeneities m_{in} (hatched patches) saturated with another fluid f_{in} (dark-shaded spherical patches). (c) ETLP model: A porous skeleton saturated with an immiscible fluid f_{out} (host fluid) contains random-sized ellipsoidal heterogeneities m_{in} (hatched patches) saturated with a second fluid f_{in} (dark-shaded ellipsoidal patches). The aspect ratio of the ellipsoids is random, but the volume fraction of the inner fluid pocket in each cell is constant.

nates, the random aspect ratio leads to ellipsoids with semimajors, randomly pointing along the horizontal and vertical directions.

DYNAMIC GOVERNING EQUATIONS OF THE ETLP MODEL

Fabric and fluid heterogeneities are taken into consideration simultaneously in the ETLP model that consists of ellipsoidal solid inclusions embedded in a homogeneous host porous medium. The matrix is partitioned into inclusions and host skeleton by the interface S_{solid} (see Figure 2). The heterogeneous skeleton has a double-porosity structure; i.e., the ellipsoidal inclusions have porosity of ϕ_{in} and the surrounding host region has porosity of ϕ_{host}. The radii of the inclusions are much smaller than the wavelength but much larger than the pore size (at a mesoscopic scale). The interface between the inclusions and the host medium is open, and the fluids can flow through it. The host region is approximated by an equivalent concentric ellipsoidal shell. Similar to White's (1975) model for a periodic heterogeneity, a typical representative elementary volume (REV) is analyzed. An ellipsoidal solid heterogeneity is located at the center. The REV is saturated with two immiscible fluids that form an inner ellipsoidal core and an outer concentric ellipsoidal shell. It is assumed that the center of the fluid overlaps with that of the solid heterogeneity. The dynamic formulation developed for the REV is considered a representation of the macroscopic mean response. Based on such approximations, analytical solutions are obtained by deriving differential equations and measurable coefficients.

The double-porosity skeleton is saturated with two immiscible fluids separated by the interface S_{fluid}. Therefore, the fabric structure and pore fluid patches are two independent heterogeneous systems and need to be treated separately. Consequently, the domain saturated with the inner fluid pocket may include the skeletons composed of the two porous components. On the other hand, the host fluid can also saturate the two porous components when the volume represented by S_{fluid} is smaller than that of S_{solid}.

The configurations of the fluid interface S_{fluid} and solid interface S_{solid} are as follows: (1) S_{fluid} is located inside S_{solid} and (2) S_{solid} is located inside S_{fluid} (Sun et al., 2016). Then, a new formulation is proposed to incorporate the fluid and solid heterogeneities simultaneously.

If the region saturated with one fluid covers two types of porous components, the effective porosity in such a region will be used for the formulation. The function $\begin{bmatrix}\phi_{\text{in}}\\ \phi_{\text{host}}\end{bmatrix}_{\text{fluid}}$ indicates the effective porosities of the region covered by the inner fluid pocket and the surrounding fluid patch, respectively. The relationships between the effective and intrinsic porosities are

$$\begin{bmatrix}\phi_{\text{in}}\\ \phi_{\text{host}}\end{bmatrix}_{\text{fluid}} = \mathbf{G}\cdot\begin{bmatrix}\phi_{\text{in}}\\ \phi_{\text{host}}\end{bmatrix}_{\text{solid}}, \tag{1}$$

where

$$\mathbf{G} = \delta v\begin{bmatrix}\frac{v_s}{\delta v} & H(\delta v)\\ -H(\delta v) & \frac{1-v_1}{\delta v}+H(\delta v)\end{bmatrix}, \tag{2}$$

where $H(\delta v)$ is the Heaviside function,

$$H(\delta v) = \begin{cases}0 & \delta v < 0\\ 1 & \delta v \geq 0\end{cases}, \tag{3}$$

and $\delta v = v_1 - v_s$, with v_1 and v_s being the volume fractions of the inner fluid pocket and solid inclusion, respectively.

In the same way, the effective permeability can be determined by

$$\langle\kappa_{\text{in}}\rangle^{-1} = \kappa_{\text{in}}^{-1}v_s + \kappa_{\text{host}}^{-1}H(v_1-v_s)\times(v_1-v_s), \tag{4}$$

$$\langle\kappa\rangle_{\text{host}}^{-1} = \kappa_{\text{host}}^{-1}(1-v_1) + (\kappa_{\text{host}}^{-1}-\kappa_{\text{in}}^{-1})H(v_1-v_s)\times(v_1-v_s). \tag{5}$$

The fluid pocket is assumed to have an ellipsoidal surface with the initial principal radii (a_0, b_0, c_0) (Figure 3). The instantaneous radii are (a, b, c) when the P-wave oscillation causes LFF. Using the ellipsoidal coordinates (r, θ, ψ), the distance from the origin point to a point on the ellipsoidal surface is

$$r = (a^2\cos^2\psi\sin^2\theta + b^2\sin^2\psi\sin^2\theta + c^2\cos^2\theta)^{1/2}, \tag{6}$$

where $\psi \in [0, 2\pi]$, $\theta \in [0, \pi]$. In the case that the fluid pocket is exposed to anisotropic hydrostatic pressure, the pocket expands and shrinks, keeping its original shape. Then, we have $a/a_0 = b/b_0 = c/c_0 = r/r_0$.

By considering wave-induced flow at the fluid surface, the fluid being depleted from the inner pocket to the outer shell is $\phi_1\zeta$, and the opposite flow induces the variation $-\phi_2\zeta$, where ζ is the variation of fluid content, which allows for fluid mass conservation in the system:

$$\zeta = \frac{1}{\phi_2}\left(1-\frac{a_{10}b_{10}c_{10}}{a_1b_1c_1}\right) = \frac{1}{\phi_2}\left(1-\frac{a_{10}^3}{a_1^3}\right). \tag{7}$$

Here, a_{10}, b_{10}, c_{10} are the initial principal radii of the inner fluid pocket and a_1, b_1, c_1 are the instantaneous radii of the inner fluid pocket when the P-wave oscillation causes LFF. We introduce the following notation:

$$\phi_1 = \langle\phi\rangle_{\text{in}} = \phi_{10}v_1, \tag{8}$$

$$\phi_2 = \langle\phi\rangle_{\text{host}} = \phi_{20}(1-v_1). \tag{9}$$

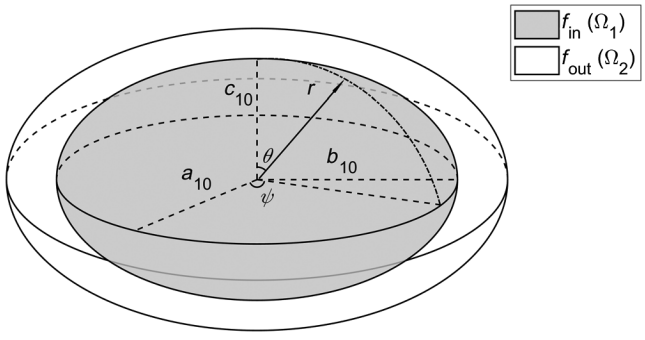

Figure 3. Schematic diagram of an ellipsoidal fluid pocket and the corresponding surrounding fluid patch. Here, a_{10}, b_{10}, and c_{10} are the initial principal radii.

For a double-porosity dual-fluid system with ellipsoidal heterogeneities, the dynamic governing equations can be derived using the Euler-Lagrange equations including the dissipation functions

$$\frac{\partial}{\partial t}\left(\frac{\partial L}{\partial \dot{u}_i}\right)+\sum_{j=1}^{3}\frac{\partial}{\partial x_j}\left(\frac{\partial L}{\partial u_{i'j}}\right)+\frac{\partial L}{\partial u_i}+\frac{\partial (D+D_L)}{\partial \dot{u}_i}=0, \tag{10}$$

$$\frac{\partial}{\partial t}\left(\frac{\partial L}{\partial \dot{\zeta}}\right)+\frac{\partial L}{\partial (\zeta)}+\frac{\partial (D+D_L)}{\partial \dot{\zeta}}=0, \tag{11}$$

where $L=T-W$. The kinetic energy T is

$$T=\frac{1}{2}\sum_{i=1}^{3}\rho_{00}\dot{u}_i^2+\sum_{i=1}^{3}\sum_{m=1}^{2}\rho_{0m}\dot{u}_i\dot{U}_i^{(m)} +\frac{1}{2}\sum_{i=1}^{3}\sum_{m=1}^{2}\rho_{mm}\dot{U}_i^{(m)2}+\frac{\phi_1\phi_2^2}{6}\dot{\zeta}^2\chi_1, \tag{12}$$

where $U_i^{(m)}$ is the fluid displacement in the mth fluid region. Here, $m=1$ denotes the inner fluid pocket, $m=2$ is the surrounding shell, and u_i is the mesoscopic volume average displacement of the solid skeleton. It is assumed that the concentric ellipsoidal fluid patches have random sizes (see Figure 1c). The radii of the ith type of ellipsoidal patch size are (a_{i10}, b_{i10}, c_{i10}), and the results are frequency dependent and depend on the patch size. This can be related to the unit cell defined by White (1975), which is composed of a core and an outer shell. The patch size is physically determined by the gas pocket size and the saturation. In the ETLP model, the patch is ellipsoidal and triple layered. The last term in the kinetic energy is related to the LFF at the fluid interface (Appendix A), where

$$\chi_1=\left(\rho_{f_1}\frac{1}{n}\sum_{i=1}^{n}a_{i10}^2E_1+\rho_{f_2}\frac{\phi_{10}}{\phi_{20}}\frac{1}{n}\sum_{i=1}^{n}a_{i10}^2E_2\right), \tag{13}$$

$$E_1=\int_{\psi_0=0}^{2\pi}\int_{\theta_0=0}^{\pi}(\sin^2\theta_0\cos^2\psi_0+r_{ba}^2\sin^2\theta_0\sin^2\psi_0+r_{ca}^2\cos^2\theta_0)^{\frac{3}{2}} \times(r_{ca}^{-2}\cos^2\theta_0+r_{ba}^{-2}\sin^2\psi_0\sin^2\theta_0+\cos^2\psi_0\sin^2\theta_0)^{\frac{1}{2}} \times Y_l^h(\theta_0,\psi_0)Y_l^{\bar{h}}(\theta_0,\psi_0)\sin\theta_0 d\theta_0 d\psi_0, \tag{14}$$

$$E_2=\frac{1}{3}\left(1+\frac{b_{10}^2}{a_{10}^2}+\frac{c_{10}^2}{a_{10}^2}\right)\left(1-\frac{a_{10}}{a_{20}}\right), \tag{15}$$

where $r_{ba}=b_{10}/a_{10}$ and $r_{ca}=c_{10}/a_{10}$. Here, $Y_l^h(\theta_0,\psi_0)$ are Laplace's spherical harmonics of degree l and order h. The total number of the different principal radii is n.

The density coefficients are (Ba et al., 2011; Sun et al., 2016)

$$\rho_{mm}=\frac{\rho_{f_m}}{2}\phi_m\left(1+\frac{1}{\phi_{m0}}\right), \tag{16}$$

$$\rho_{0m}=\frac{\rho_{f_m}}{2}\phi_m\left(1-\frac{1}{\phi_{m0}}\right), \tag{17}$$

$$\rho_{00}=\rho_0-\frac{1}{2}\sum_{m=1}^{2}\rho_{f_m}\phi_m\left(1-\frac{1}{\phi_{m0}}\right), \tag{18}$$

where $\rho_0=\sum_{m=1}^{2}v_m(1-\phi_{m0})\rho_{s_m}$ is the density of the dry skeleton, ρ_{f_m} are the fluid densities of the mth fluid patch, and $v_2=1-v_1$ is the volume fraction of the surrounding shell of fluid patch.

The strain energy W is

$$W=\frac{1}{2}[(A+2N)I_1^2-4NI_2+2Q_1I_1(\xi_1-\phi_2\zeta)+R_1(\xi_1-\phi_2\zeta)^2 +2Q_2I_1(\xi_2+\phi_1\zeta)+R_2(\xi_2+\phi_1\zeta)^2], \tag{19}$$

where I_1 and I_2 are the first and second strain invariants of the solid phase, ξ_m are the fluid dilatations of the fluid displacements $\mathbf{U}^{(m)}(m=1,2)$, N is the effective shear modulus of the whole solid skeleton, and A, Q_m, R_m $(m=1,2)$ are the stiffness coefficients.

The dissipation function D is

$$D=\frac{1}{2}\sum_{m=1}^{2}b_m\sum_{i=1}^{3}(\dot{U}_i^{(m)}-\dot{u}_i)^2+\frac{\phi_1\phi_2^2}{6}\dot{\zeta}^2\beta_1, \tag{20}$$

where $b_m=v_m\phi_{m0}^2(\eta_m/\kappa_m)$ $(m=1,\ 2)$ is the Biot's dissipation coefficients, κ_m is the permeability of each component, and η_m and v_m are the viscosity and volume fraction of each phase, respectively. The notations $\kappa_1=\langle\kappa\rangle_{\text{in}}$ and $\kappa_2=\langle\kappa\rangle_{\text{host}}$ are introduced.

The last term in dissipation function is caused by LFF, where

$$\beta_1=\phi_{10}\left(\frac{\eta_1}{\kappa_1}\frac{1}{n}\sum_{i=1}^{n}a_{i10}^2E_1+\frac{\eta_2}{\kappa_2}\frac{1}{n}\sum_{i=1}^{n}a_{i10}^2E_2\right). \tag{21}$$

The dynamic equations are

$$\begin{aligned}
&\rho_{00}\ddot{\mathbf{u}}+\sum_{m=1}^{2}[\rho_{0m}\ddot{\mathbf{U}}^{(m)}+b_m(\dot{\mathbf{u}}-\dot{\mathbf{U}}^{(m)})]=N\nabla^2\mathbf{u}+(A+N)\nabla I_1\\
&+Q_1\nabla(\nabla\cdot\mathbf{U}_1-\phi_2\zeta)+\mathbf{Q}_2\nabla(\nabla\cdot\mathbf{U}_2+\phi_1\zeta)\\
&\rho_{01}\ddot{\mathbf{u}}+\rho_{11}\ddot{\mathbf{U}}^{(1)}+b_1(\dot{\mathbf{U}}^{(1)}-\dot{u})=Q_1\nabla(\nabla\cdot\mathbf{u})+R_1\nabla(\nabla\cdot\mathbf{U}_1-\phi_2\zeta)\\
&\rho_{02}\ddot{\mathbf{u}}+\rho_{22}\ddot{\mathbf{U}}^{(2)}+b_2(\dot{\mathbf{U}}^{(2)}-\dot{u})=Q_2\nabla(\nabla\cdot\mathbf{u})+R_2\nabla(\nabla\cdot\mathbf{U}_2+\phi_1\zeta)\\
&-(\chi_1\ddot{\zeta}_1+\beta_1\dot{\zeta}_1)\frac{\phi_1\phi_2^2}{3}=\phi_2[Q_1\nabla(\nabla\cdot\mathbf{u})+R_1\nabla(\nabla\cdot\mathbf{U}_1-\phi_2\zeta)]\\
&-\phi_1[Q_2\nabla(\nabla\cdot\mathbf{u})+R_2\nabla(\nabla\cdot\mathbf{U}_2+\phi_1\zeta)],
\end{aligned} \tag{22}$$

where $\zeta=\nabla\cdot\mathbf{Z}$ is the increment of LFF caused by the pressure gradient between different fluid patches, $\mathbf{Z}$ is the LFF between the immiscible fluid patches, and $\mathbf{e}$ is the strain. The Biot dissipation coefficients can also be written as $b_m=\rho_{f_m}\phi_m\omega_c^{(m)}$ $(m=1,\ 2)$, where $\omega_c^{(m)}=\mu_m\phi_{m0}/\rho_{f_m}\kappa_m$ are the characteristic frequencies for immiscible fluid patches.

Using a harmonic-wave analysis, we substitute the solution $e^{i(\omega t-kx)}$ in the solid and fluid displacements of the wave equations,

where ω and k are the angular frequency and wavenumber, respectively. Then, we have

$$\begin{bmatrix} a_{11}Y + b_{11}a_{12}Y + b_{12}a_{13}Y + b_{13} \\ a_{21}Y + b_{21}a_{22}Y + b_{22}a_{23}Y + b_{23} \\ a_{31}Y + b_{31}a_{32}Y + b_{32}a_{33}Y + b_{33} \end{bmatrix} \begin{Bmatrix} C_1 \\ C_2^{(1)} \\ C_2^{(2)} \end{Bmatrix} = 0, \quad (23)$$

where $Y = (k/\omega)^2$, $m = 1, 2$. Equation 23 has nonzero solutions for $C_1, C_2^{(1)}, C_2^{(2)}$, only if the determinant is zero, which yields

$$AY^3 + BY^2 + CY + D = 0. \quad (24)$$

The coefficients a_{ij}, b_{ij} and A, B, C, D are given in Appendix B. This equation in $(k/\omega)^2$ has three roots, corresponding to the fast P-wave and two slow P-waves. The complex and phase P-wave velocities are, respectively, defined as $v = \omega/k$ and $V_P = 1/(\mathrm{Re}(1/v))$. The P-wave dissipation factor is obtained as $Q^{-1} = (\mathrm{Im}(v^2))/(\mathrm{Re}(v^2))$.

NUMERICAL EXAMPLES

Effects of aspect ratio on velocity dispersion and attenuation in a tight sandstone

We first consider the effects of the aspect ratio of the ellipsoidal inhomogeneities in a Fort Union sandstone, which has an average grain size between 0.125 and 0.15 mm (Murphy, 1984). Table 1 shows the rock and fluid properties.

Figures 4 and 5 show the acoustic phase velocity dispersion and attenuation in Fort Union sandstone as a function of water saturation at a frequency of 5Hz, 100 Hz, 5 kHz, and 1 MHz and a patch size $a = 1.2$ mm (semi-major axis). The semi-minor axis radii are set as $b = a \cdot r_{ba}$ and $c = a \cdot r_{ca}$ (for simplicity, $r_{ca} = 1$). In natural rocks, the fluid patch shapes are not spheres (Tserkovnyak and Johnson, 2002). The geometry depends on the experimental conditions, such as fluid injection rate, open/close boundaries, etc. Laboratory observations have confirmed that the P-wave velocity may be quite different even for the same saturation, which is caused by different fluid patch geometries induced by different injection rates (Lebedev et al., 2009; Liu et al., 2016). As shown in Figures 4 and 5, the P-wave velocities at different frequencies depend on the aspect ratio of the inhomogeneities, which indicates that the fluid patch geometry must be considered to interpret velocity dispersion and attenuation phenomena.

As shown in Figure 4, the velocity-saturation relationships are highly dependent on the aspect ratio at 100 Hz and 5 KHz (when the aspect ratio approaches one, the ETLP model reduces to the TLP model of Sun et al., 2016). However, at 5 Hz, the velocity sharply increases at high water saturations (80% to almost 100%) when the aspect ratio decreases (Figure 4a). For a water saturation less than 80%, the velocity is almost constant with varying aspect ratio. On the contrary, at 1 MHz, the velocity increases with decreasing aspect ratio at low water saturations (0%–60%) (Figure 4d).

Figure 5 shows that the P-wave attenuation is also sensitive to the aspect ratio. In general, the attenuation peak shifts to the low water saturations with decreasing aspect ratio. At 5 Hz in Figure 5a, the attenuation is significant in the water saturation range >60%, whereas at 100 Hz in Figure 5b, this occurs in the range >40%. It is also shown that at the same frequency, a lower attenuation peak can be observed with decreasing aspect ratio, and the attenuation is low at 1 MHz and aspect ratio 0.1 in Figure 5d.

Table 1. Rock and fluid properties for the Fort Union sandstone (Murphy, 1984).

Property	Value
ϕ	0.085
K_s (GPa)	35.00
K_b (GPa)	7.14
N_b (GPa)	9.06
ρ_s (kg/m^3)	2650
κ (m^2)	0.5×10^{-15}
K_{water} (GPa)	2.25
ρ_{water} (kg/m^3)	997
η_{water} (Pa · s)	0.001
K_{gas} (MPa)	0.8
ρ_{gas} (kg/m^3)	100
η_{gas} (Pa s)	1.00×10^{-5}

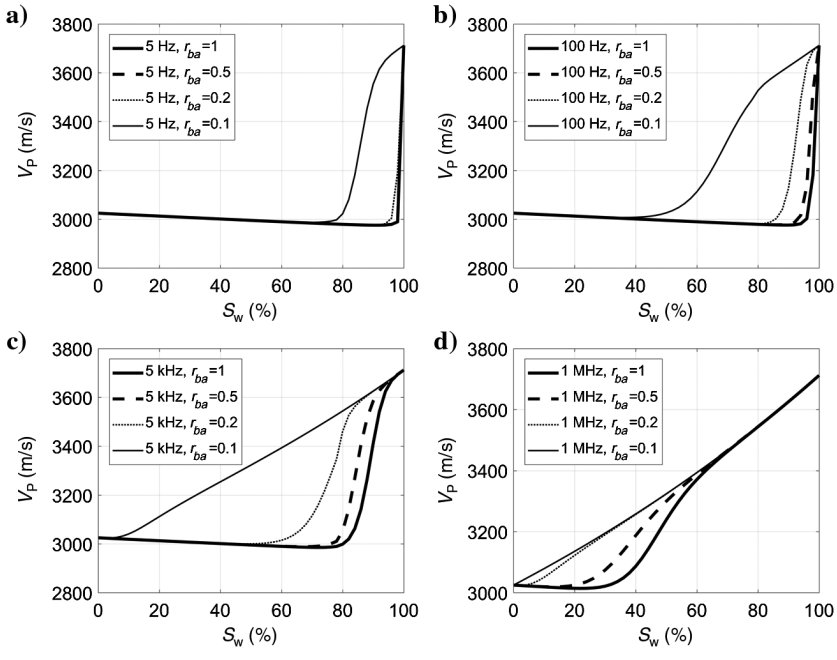

Figure 4. The P-wave velocity as a function of water saturation in Fort Union sandstone predicted by the ETLP model. The aspect ratios of the ellipsoidal inhomogeneities are 1, 0.5, 0.2, and 0.1. (a-d) Correspond to frequencies of 5 Hz, 100 Hz, 5 kHz, and 1 MHz, respectively.

High-porosity sandstone at sonic frequencies

The effects of ellipsoidal patches on the velocity-saturation relationship are investigated by comparison to laboratory data of a North Sea sandstone, with a porosity of 35% and a permeability of 8.7D, at several frequencies. The rock properties are given in Table 2 (Boruah and Chatterjee, 2010).

The rock-skeleton bulk and shear moduli K_b and N are obtained as $K_b=(K_s(1-\phi))/(1+\alpha\phi)$ and $N=(N_s(1-\phi))/(1+1.5\alpha\phi)$ (Cadoret et al., 1998; Han et al., 2007). The dry-rock velocities of the sandstone are fitted to determine the consolidation parameter α.

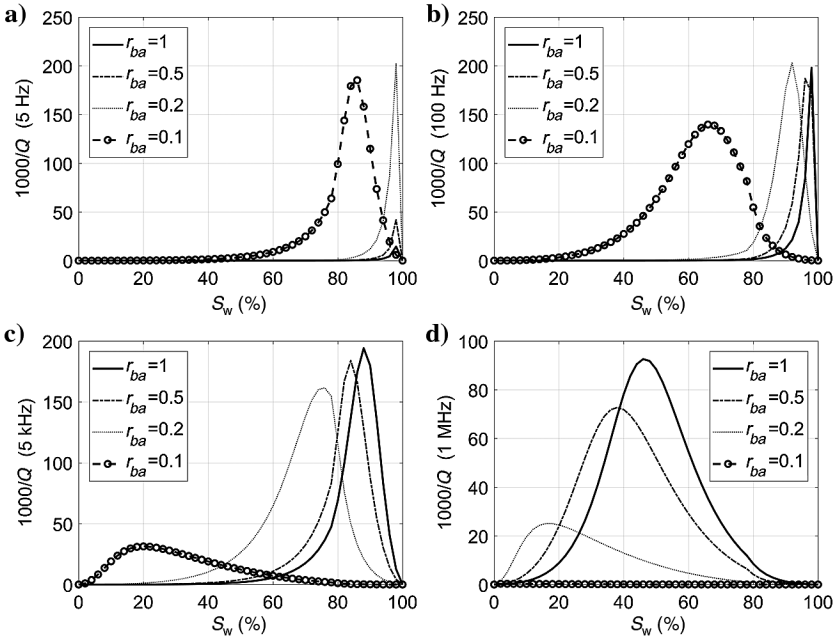

Figure 5. P-wave attenuation as a function of water saturation in Fort Union sandstone predicted by the ETLP model. The aspect ratios of the ellipsoidal inhomogeneities are 1, 0.5, 0.2, and 0.1. (a-d) Correspond to frequencies of 5 Hz, 100 Hz, 5 kHz, and 1 MHz, respectively.

Table 2. Rock and fluid properties of a North Sea sandstone (Boruah and Chatterjee, 2010).

Property	Value
ϕ	0.35
K_s (GPa)	39.47
ρ_s (kg/m^3)	2630
N (GPa)	36.61
κ (m^2)	8.586×10^{-12}
K_{brine} (GPa)	2.48
ρ_{brine} (kg/m^3)	1060
η_{brine} (Pa s)	0.0011
K_{gas} (GPa)	1.01×10^{-5}
ρ_{gas} (kg/m^3)	1.2
η_{gas} (Pa s)	1.81×10^{-5}

The North Sea sandstone is predominantly composed of quartz with clay coating the mineral grains (Avseth, 2000). The quartz cementation is inhibited by the clay and organic matter coating the solid grains. The clay content in the pore system results in a great number of small contact cracks. The double-porosity structure consists of low-porosity clay and high-porosity sandstone. The solid particles are usually not very rounded or polished and larger interparticle pores exist.

When a traveling wave passes through a heterogeneous rock, a pore pressure gradient is generated due to the spatial variations of the pore shape/structure, pore stiffness, and fluid saturation. Fluid flow occurs across the interface between the patch and the host phase, which equilibrates pressure differences at a local scale and causes velocity dispersion and attenuation. The pressure equilibration of the pore fluid depends on LFF, which in turn depends on the patch size and diffusion length. For a low-frequency wave, the diffusion length can be much larger than the fluid patch size. Then, the pore fluid pressure equilibrates between the different phases in each wave circle, and the Gassmann-Wood's model is a reliable approximation (Müller et al., 2010). At the high-frequency limit, the unrelaxed local fluid pressure will strengthen the elastic stiffness of the porous matrix. Gassmann-Hill's model is used to calculate the upper limit of the frame velocity.

The patch size can be characterized by the volume-surface area ratio (Tserkovnyak and Johnson, 2002). For ellipsoidal heterogeneous inclusions, the volume-surface area ratio is a function of the three radii corresponding to the different semiaxes, which in turn depend on the aspect ratio. The range of fluid patch sizes can be determined from the average grain size and estimating the diffusion length (Sun et al., 2016). In this work, the aspect ratio of the ellipsoidal patch provides another degree of freedom to characterize the effect of the LFF.

We calculated the P-wave dispersion and attenuation on the basis of the patch geometry and inclusion volume fractions. The Biot-Gassmann-Wood (BGW) and Biot-Gassmann-Hill (BGH) limits (Ba et al., 2015) are also given as a reference. The aspect ratio of the ellipsoidal heterogeneities is 1 (Figure 6) and 0.001 (Figure 7). It is shown that the aspect ratio affects the P-wave velocities. The predicted velocities at 500 kHz significantly increase when the aspect ratio decreases from 1 to 0.001, especially for water saturations in the range of 10%–90%. At a sonic frequency of 50 kHz, the velocities also increase with decreasing aspect ratio (the P-wave velocity at $S_w = 80\%$ increases approximately by 100 m/s). At a seismic frequency of 50 Hz, the velocities at high water saturation (approximately 90%) decrease with the decreasing aspect ratio.

Figure 6 shows the modeling results with spherical heterogeneities (aspect ratio equal to one; the ETLP model reduces to the TLP model of Sun et al., 2016). The aspect ratio 0.001 can better describe the 500 kHz experimental data (see Figure 7). The TLP model with spherical inclusions cannot describe the strong stiffening effects at ultrasonic frequencies observed in the data of

Batzle et al. (2006). Furthermore, the Gassmann model is only effective at the low-frequency limit, i.e., when there are no pressure gradients in the pore fluid. It is not applicable at higher frequencies, in which the Biot and local fluid mechanisms should be considered. By modeling flat heterogeneities and double-porosity/dual-fluid characteristics, the ETLP provides a better fit of the experimental data than the BGH model.

The unexpected high values of the ultrasonic velocities were previously ascribed to sample heterogeneity (Batzle et al., 2006). There is an inflection point in the ultrasonic experimental data at water saturations of approximately 80%. The North Sea sandstone has high porosity (35%) and high permeability (8.7D). The sharp increase of velocity versus saturation in the saturation range >80% could be related to the different geometric features of the fluid patches between the low and high water saturations. In the ETLP modeling, a single set of parameters regarding the patch size and shape is used, which cannot fully describe the observed velocity at each saturation. However, it is able to explain the general trend and characteristics of the velocity-saturation relationship.

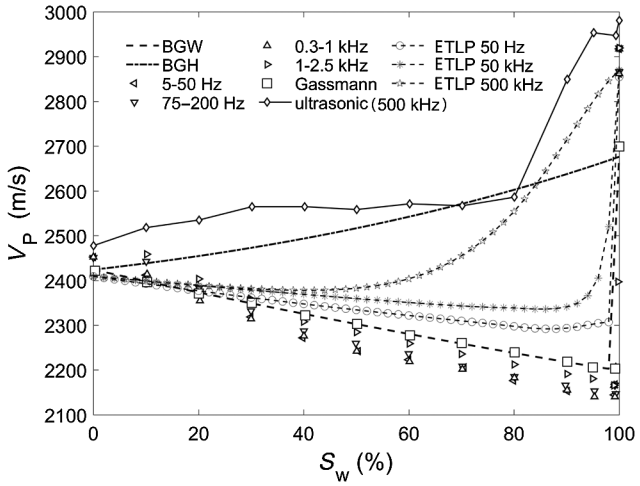

Figure 6. Measured and theoretically predicted P-wave velocities of the North Sea sandstone. The aspect ratio of the ellipsoidal inhomogeneity is one. The symbols are experimental data from Batzle et al. (2006).

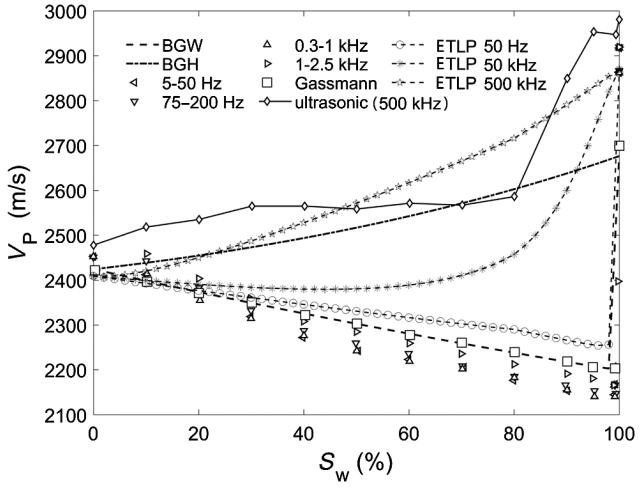

Figure 7. Measured and theoretically predicted P-wave velocities of the North Sea sandstone. The aspect ratio of the ellipsoidal inhomogeneity is 0.001. The symbols are experimental data from Batzle et al. (2006).

CONCLUSION

We propose an ETLP model to describe wave propagation in partially saturated double-porosity media. The model combines the macroscopic Biot flow and the mesoscopic LFF under the effects of ellipsoidal fluid and fabric heterogeneities. This model provides a physical approach to investigate the coupling effect between heterogeneity-geometry and wave dispersion/attenuation. The model incorporates the fluid distribution and rock structure heterogeneities from spherical to flat shapes, a wide distribution that commonly coexists in natural reservoir rocks. When the aspect ratio is one, the model reduces to the TLP model with spherical patches, which can then further be reduced to the classic Biot theory. For small aspect ratios, we can model the effects of cracks. An analysis of the effects of frequency and ellipsoidal aspect ratio based on numerical examples reveals that the aspect ratio is an essential parameter that controls the observed dispersion and attenuation. It is concluded that the agreement between the predicted velocity and experiment data is reasonably good because of the more flexible geometry of the present model, which can be applied to partially saturated fractured porous reservoirs and allows for a broader insight on the related wave phenomena because it considers inclusions of flat shapes. Because we have developed the model from first principles (Lagrange equations), we also have obtained the governing differential equations of wave propagation that can be used to compute synthetic seismograms.

ACKNOWLEDGMENTS

We wish to thank the editor C. Torres-Verdin, the associate editor Y. Li, J. Deeks, and the two anonymous reviewers for the rigorous reviews of this work, which helped to improve the paper. This research was sponsored by the Foundation of the State Key Laboratory of Petroleum Resources and Prospecting, China University of Petroleum, Beijing (no. PRP/open-1511), the Distinguished Professor Program of Jiangsu Province, China, and the open fund of the State Key Laboratory of the Institute of Geodesy and Geophysics, CAS (SKLGED2017-5-2-E).

APPENDIX A

KINETIC ENERGY OF LFF

The velocity field in the fluid pocket is obtained from

$$\rho_{f_1} \frac{\partial \dot{\mathbf{r}}}{\partial t} = -\nabla p, \tag{A-1}$$

where p is the pressure. The density ρ_{f_1} is assumed constant. The pressure can be obtained in spherical coordinates as (Buivol, 2006)

$$p = \sum_{l=0}^{\infty} \sum_{h=-l}^{l} c_{lh}(t) \frac{r_0^l}{r_{10}^l} Y_l^h(\theta_0, \psi_0), \tag{A-2}$$

where r_0 ($r_0 < r_{10}$) is the instantaneous distance from an arbitrary point on the ellipsoid fluid pocket surface to the origin point, r_{10} is

the static radius of the fluid pocket, c_{lh} are the coefficients of the mathematical expansion, and $Y_l^h(\theta_0, \psi_0)$ are the Laplace spherical harmonics of degree l and order h. By combining the above two equations, the fluid displacement is

$$\mathbf{r} = \mathbf{r_0} + \sum_{l,h} r_{lh}(t) r_{10} \nabla \left(\frac{r_0^l}{r_{10}^l} Y_l^h(\theta_0, \psi_0) \right). \tag{A-3}$$

The unperturbed fluid element position is $\mathbf{r_0}$ and the position coefficients r_{lh} satisfy $\dot{r}_{lh} = -(1/\rho_{f_1} r_{10}) \int c_{lh}(t) dt$. In the case of irrotational vibrations, the displacement gradient is independent of θ_0, ψ_0, and $\nabla = d/dr_0$. At the surface of the fluid pocket, the radial displacement component is given by

$$r_1 = r_{10} + \sum_{l,h} r_{lh}(t) l Y_l^h(\theta_0, \psi_0), \tag{A-4}$$

where $r_{10} = \sqrt{a_{10}^2 \sin^2\theta \cos^2\psi + b_{10}^2 \sin^2\theta \sin^2\psi + c_{10}^2 \cos^2\theta}$ is the distance from a point on S_{fluid} to the origin point. The final kinetic energy of the inner fluid pocket is

$$\begin{aligned}
&\frac{1}{2}\phi_{10} \int_{\Omega_1} \rho_{f_1} \dot{\mathbf{r}} \cdot \dot{\mathbf{r}} d\Omega_1 \\
&= \frac{1}{2}\phi_{10} \int_{\Omega_1} \rho_{f_1} \left[\sum_{l,h} \dot{r}_{lh}(t) r_1 \nabla \left(\frac{r_0^l}{r_1^l} Y_l^h(\theta_0, \psi_0) \right) \right. \\
&\quad \left. \cdot \sum_{\bar{l},\bar{h}} \dot{r}_{\bar{l}\bar{h}}(t) r_1 \nabla \left(\frac{r_0^{\bar{l}}}{r_1^{\bar{l}}} Y_{\bar{l}}^{\bar{h}}(\theta_0, \psi_0) \right) \right] d\Omega_1 \\
&= \frac{1}{2}\phi_{10} \int_{\partial\Omega_1} \rho_{f_1} \left[\sum_{l,h} \dot{r}_{lh}(t) r_1 \left(\frac{r_0^l}{r_1^l} Y_l^h(\theta_0, \psi_0) \right) \right. \\
&\quad \left. \cdot \frac{\partial}{\partial r_0} \left(\sum_{\bar{l},\bar{h}} \dot{r}_{\bar{l}\bar{h}}(t) r_1 \left(\frac{r_0^{\bar{l}}}{r_1^{\bar{l}}} Y_{\bar{l}}^{\bar{h}}(\theta_0, \psi_0) \right) \right) \right] dS_0 \\
&= \frac{1}{2}\phi_{10}\rho_{f_1} \sum_{l,h} \sum_{\bar{l},\bar{h}} \bar{l} \int_{\theta_0=0}^{\pi} \int_{\psi_0=0}^{2\pi} \dot{r}_{lh} \dot{r}_{\bar{l}\bar{h}} r_1 \tilde{r}(\theta_0, \psi_0)^2 \\
&\quad \times Y_l^h(\theta_0, \psi_0) Y_{\bar{l}}^{\bar{h}}(\theta_0, \psi_0) \sin\theta_0 d\theta_0 d\phi_0,
\end{aligned} \tag{A-5}$$

where $\tilde{r}(\theta_0,\psi_0)^2 = \sqrt{a_1^2 b_1^2 \cos^2\theta_0 + a_1^2 c_1^2 \sin^2\psi_0 \sin^2\theta_0 + b_1^2 c_1^2 \cos^2\psi_0 \sin^2\theta_0}$. Note that $r_0 = r_{10}$ on the ellipsoidal surface and $dS_0 = \tilde{r}^2 \sin\theta_0 \, d\theta_0 d\psi_0$. By considering the proportional deformation relationships $a/a_0 = b/b_0 = c/c_0 = r/r_0$,

$$\tilde{r}^2 = a_1^2 \sqrt{\frac{b_{10}^2}{a_{10}^2}\cos^2\theta_0 + \frac{c_{10}^2}{a_{10}^2}\sin^2\psi_0 \sin^2\theta_0 + \frac{b_{10}^2 c_{10}^2}{a_{10}^4}\cos^2\psi_0 \sin^2\theta_0}. \tag{A-6}$$

The kinetic energy of the inner sphere is then

$$\begin{aligned}
T_L^{(1)} &= 2\pi\rho_{f_1}\phi_{10} \int_{\theta_0=0}^{\pi} \int_{\psi_0=0}^{2\pi} \frac{r_{10} a_1}{a_{10}} \left(\frac{r_{10}\dot{a}_1}{a_{10}} \right)^2 \\
&\quad \times \tilde{r}^2 Y_l^h(\theta_0, \psi_0) Y_{\bar{l}}^{\bar{h}}(\theta_0, \psi_0) \sin\theta_0 d\theta_0 d\psi_0 \\
&= 2\pi\rho_{f_1}\phi_{10} a_1^3 \dot{a}_1^2 \int_{\theta_0=0}^{\pi} \int_{\psi_0=0}^{2\pi} \frac{r_{10}^3}{a_{10}^3} \left(\frac{b_{10}^2}{a_{10}^2}\cos^2\theta_0 \right. \\
&\quad \left. + \frac{c_{10}^2}{a_{10}^2}\sin^2\psi_0 \sin^2\theta_0 + \frac{b_{10}^2 c_{10}^2}{a_{10}^4}\cos^2\psi_0 \sin^2\theta_0 \right)^{\frac{1}{2}} \\
&\quad \times Y_l^h(\theta_0, \psi_0) Y_{\bar{l}}^{\bar{h}}(\theta_0, \psi_0) \sin\theta_0 d\theta_0 d\psi_0 \\
&= 2\pi\rho_{f_1} a_1^3 r_{ba} r_{ca} \dot{a}_1^2 \phi_{10} E_1,
\end{aligned} \tag{A-7}$$

$$\begin{aligned}
E_1 &= \int_{\psi_0=0}^{2\pi} \int_{\theta_0=0}^{\pi} (\sin^2\theta_0 \cos^2\psi_0 + r_{ba}^2 \sin^2\theta_0 \sin^2\psi_0 \\
&\quad + r_{ca}^2 \cos^2\theta_0)^{\frac{3}{2}} \\
&\quad \times (r_{ca}^{-2} \cos^2\theta_0 + r_{ba}^{-2} \sin^2\psi_0 \sin^2\theta_0 \\
&\quad + \cos^2\psi_0 \sin^2\theta_0)^{\frac{1}{2}} Y_l^h(\theta_0, \psi_0) Y_{\bar{l}}^{\bar{h}}(\theta_0, \psi_0) \sin\theta_0 d\theta_0 d\psi_0,
\end{aligned} \tag{A-8}$$

where $r_{ba} = b_{10}/a_{10}$ and $r_{ca} = c_{10}/a_{10}$. To approximately estimate E_1, we consider a case in which $r_{ba} = 1$; i.e., the radii at the x-axis and y-axis are the same. Then, E_1 can be integrated as

$$\begin{aligned}
E_1 &= \int_{\psi_0=0}^{2\pi} \int_{\theta_0=0}^{\pi} (\sin^2\theta_0 + r_{ca}^2 \cos^2\theta_0)^{\frac{3}{2}} (\sin^2\theta_0 \\
&\quad + r_{ca}^{-2} \cos^2\theta_0)^{\frac{1}{2}} Y_l^h(\theta_0, \psi_0) Y_{\bar{l}}^{\bar{h}}(\theta_0, \psi_0) \sin\theta_0 d\theta_0 d\psi_0.
\end{aligned} \tag{A-9}$$

In the case of a spherical pocket, i.e., $a_{10} = b_{10} = c_{10}$, the eigenfunctions $Y_l^h(\theta_0, \phi_0)$ are normalized to be orthonormal integrated over the surface of the unit sphere.

$$\begin{aligned}
E_1 &= \int_{\theta_0=0}^{\pi} \int_{\psi_0=0}^{2\pi} Y_l^h(\theta_0, \psi_0) Y_{\bar{l}}^{\bar{h}}(\theta_0, \psi_0) \sin\theta_0 d\theta_0 d\psi_0 \\
&= \delta(l - \bar{l}) \delta(h - \bar{h}).
\end{aligned} \tag{A-10}$$

For $l = h = 1$, $E_1 = 1$, and $T_L^{(1)} = 2\pi\rho_{f_1} a_1^3 r_{ba} r_{ca} \dot{a}_1^2 \phi_{10}$.

The kinetic energy term $T_L^{(2)}$ related to the outer concentric shell domain is obtained as follows. For an ellipsoid $x^2/a^2 + y^2/b^2 + z^2/c^2 = R^2$, the equation can be written as $X^2 + Y^2 + Z^2 = R^2$ by $X = x/a$, $Y = y/b$, and $Z = z/c$. The volume integral is

$$V = abc \iiint_{\Omega} dX dY dZ = abc \int_0^R r^2 dr \int_0^{\pi} \sin\theta d\theta \int_0^{2\pi} d\psi, \tag{A-11}$$

where $X = r \sin\theta \sin\psi$, $Y = r \sin\theta \cos\psi$, $Z = r \cos\psi$, and $dXdYdZ = r^2 \sin\theta dr d\theta d\psi$. The surface ellipsoidal fluid patch is written as $(x^2/1) + (y^2/(b_1^2/a_1^2)) + (z^2/(c_1^2/a_1^2)) = a_1^2$. In the case of an instantaneously proportional deformation relationship $\dot{r} = (\dot{a}/\dot{a}_1)\dot{r}_1$, the kinetic energy $T_L^{(2)}$ is

$$T_L^{(2)} = \frac{1}{2}\phi_{20}\rho_{f_2}\int_{\Omega_2}\dot{r}^2 dr = \frac{1}{2}\phi_{20}\rho_{f_2} \times \int_{\Omega_2}\frac{\dot{a}^2}{a_1^2}r_1^2 dr = \frac{1}{2}\phi_{20}\rho_{f_2}\frac{b_1c_1}{a_1^2}\int_{a_1}^{a_2}\frac{\dot{a}^2}{a_1^2}a^2 da \times \int_0^{\pi}\sin\theta_0\int_0^{2\pi}a_1^2\left(\sin^2\theta_0\cos^2\psi_0 + \frac{b_1^2}{a_1^2}\sin^2\theta_0\sin^2\psi_0 + \frac{c_1^2}{a_1^2}\cos^2\theta_0\right)d\psi d\theta, \quad \text{(A-12)}$$

where $r_1 = \sqrt{a_1^2\sin^2\theta\cos^2\psi + b_1^2\sin^2\theta\sin^2\psi + c_1^2\cos^2\theta}$ is used. By considering the mass conservation at the fluid interface, $\dot{r}\phi_{m0}dS = \dot{r}_1\phi_{10}dS_1 (m = 1, 2)$, $(\dot{r}/\dot{a}) = (\dot{r}_1/\dot{a}_1)$ and

$$\dot{a} = \frac{\phi_{10}dS_1}{\phi_{20}dS}\dot{a}_1 = \frac{\phi_{10}}{\phi_{20}}\dot{a}_1 \times \frac{(a_1^2b_1^2\sin^2\psi\cos^2\psi + a_1^2c_1^2\sin^4\psi + (b_1^2 - a_1^2)c_1^2\cos^2\theta\sin^4\psi)^{\frac{1}{2}}}{(a^2b^2\sin^2\psi\cos^2\psi + a^2c^2\sin^4\psi + (b^2 - a^2)c^2\cos^2\theta\sin^4\psi)^{\frac{1}{2}}} = \frac{\phi_{10}a_1^2}{\phi_{20}a^2}\dot{a}_1. \quad \text{(A-13)}$$

Then,

$$T_L^{(2)} = \frac{1}{2}\rho_{f_2}a_1^2b_1c_1\frac{\phi_{10}^2\dot{a}_1^2}{\phi_{20}}\int_{a_1}^{a_2}\frac{1}{a^2}da \times \int_0^{\pi}\sin\theta_0\int_0^{2\pi}\left(\sin^2\theta_0\cos^2\psi_0 + \frac{b_1^2}{a_1^2}\sin^2\theta_0\sin^2\psi_0 + \frac{c_1^2}{a_1^2}\cos^2\theta_0\right)d\psi d\theta = \frac{1}{2}\rho_{f_2}a_1^2b_1c_1\frac{\phi_{10}^2\dot{a}_1^2}{\phi_{20}} \times \left(\frac{1}{a_1} - \frac{1}{a_2}\right) \times \frac{4\pi}{3}\left(1 + \frac{b_1^2}{a_1^2} + \frac{c_1^2}{a_1^2}\right) = 2\pi\rho_{f_2}a_1^3r_{ba}r_{ca}\dot{a}_1^2\frac{\phi_{10}^2}{\phi_{20}}E_2. \quad \text{(A-14)}$$

By considering the proportional deformation relationship, we have $E_2 = 1/3(1 + (b_{10}^2/a_{10}^2) + (c_{10}^2/a_{10}^2))(1 - (a_{10}/a_{20})) = 1/3(1 + (b_{10}^2/a_{10}^2) + (c_{10}^2/a_{10}^2))(1 - v_1^{1/3})$, where a_{20} is the radius of the outer patch.

In the case of a spherical pocket, $E_2 = (1 - (a_{10}/a_{20})) = (1 - v_1^{1/3})$ and $T_L^{(2)} = 2\pi\rho_{f_2}a_1^3\dot{a}_1^2(\phi_{10}^2/\phi_{20})(1 - v_1^{1/3})$.

Then, the local kinetic energy related to the ellipsoidal fluid patch inclusions is

$$T_L = T_L^{(1)} + T_L^{(2)} = 2\pi a_1^3r_{ba}r_{ca}\dot{a}_1^2\phi_{10}\left(\rho_{f_1}E_1 + \rho_{f_2}\frac{\phi_{10}}{\phi_{20}}E_2\right). \quad \text{(A-15)}$$

Suppose that there are N_0 concentric ellipsoidal fluid patches with n types of principal radii in a unit volume. The number of fluid patches with radius of the i-type $(a_{i20}, b_{i20}, c_{i20})$ is N_i; then, a probability is defined as $p_i = (N_i/N_0)$. The total volume of the fluid pockets in the unit volume is

$$N_0\sum_{i=1}^{n}\frac{4\pi}{3}a_{i2}b_{i2}c_{i2}p_iv_1 = N_0\sum_{i=1}^{n}\frac{4\pi}{3}a_{i2}^3r_{ba}r_{ca}p_iv_1 = N_0\sum_{i=1}^{n}\frac{4\pi}{3}a_{i1}^3r_{iba}r_{ica}p_i = \frac{\phi_1}{\phi_{10}}, \quad \text{(A-16)}$$

where $\phi_1 = v_1\phi_{10}$ and v_1 is the volume fraction of the inner fluid pockets. If $a_{i1}^3r_{iba}r_{ica}p_i = c$, where c is a constant,

$$a_{i1}^3r_{iba}r_{ica}p_i = \frac{3\phi_1}{N_04\pi\phi_{10}n}. (A-17) \quad \text{(A-17)}$$

By considering the wave-induced fluid flow at the fluid interface, the depleted fluid from the inner pocket to the outer domain is $\phi_1\zeta$, and the opposite flow has a content variation $-\phi_2\zeta$, where $\zeta = 1/\phi_2(1 - (a_{10}b_{10}c_{10}/a_1b_1c_1)) = 1/\phi_2(1 - (a_{10}^3/a_1^3))$. In the case of small amplitude oscillations of the fluid interfaces, the radius a_1 can be derived as $a_1 = a_{10}(1 - \phi_2\zeta)^{-\frac{1}{3}} \approx a_{10} + (1/3)a_{10}\phi_2\zeta$.

Then

$$\dot{a}_1 = \frac{1}{3}a_{10}\phi_2\dot{\zeta}. \quad \text{(A-18)}$$

The total kinetic energy of LFF of the N_0 ellipsoid fluid patches is

$$T_L = N_0\sum_{i=1}^{n}2\pi a_{i1}^3r_{iba}r_{ica}p_i\dot{a}_{i1}^2\phi_{10}\left(\rho_{f_1}E_1 + \rho_{f_2}\frac{\phi_{10}}{\phi_{20}}E_2\right), = \sum_{i=1}^{n}\frac{3\phi_1\left(\frac{1}{3}a_{i10}\phi_2\dot{\zeta}\right)^2}{2n}\left(\rho_{f_1}E_1 + \rho_{f_2}\frac{\phi_{10}}{\phi_{20}}E_2\right), = \frac{\phi_1\phi_2^2}{6}\dot{\zeta}^2\chi_1, \quad \text{(A-19)}$$

where $\chi_1 = (\rho_{f_1}\frac{1}{n}\sum_{i=1}^{n}a_{i10}^2E_1 + \rho_{f_2}\frac{\phi_{10}}{\phi_{20}}\frac{1}{n}\sum_{i=1}^{n}a_{i10}^2E_2)$ or $\chi_1 = v_1^{2/3}(\rho_{f_1}\frac{1}{n}\sum_{i=1}^{n}a_{i20}^2E_1 + \rho_{f_2}\frac{\phi_{10}}{\phi_{20}}\frac{1}{n}\sum_{i=1}^{n}a_{i20}^2E_2)$. The term v_1 is the fluid volume fraction and a_{20} is the radius of overall patch.

In deriving equation A-19, it is assumed that the radius a_{i20} and aspect ratios r_{iba}, r_{ica} of the ith type of ellipsoidal patches satisfy

$$a_{i2}^3r_{iba}r_{ica} = \frac{3}{N_in4\pi}, \quad \text{(A-20)}$$

where N_i, is the number of ellipsoidal patches with radius of a_{i2} and the corresponding aspect ratios r_{iba}, r_{ica}, and n is the number of random-sized patches in a unit volume. Because the total volume of patches with aspect ratios r_{ca}, r_{ba} is $V_i = N_i(4\pi/3)a_{i2}^3r_{iba}r_{ica}$, equation A-20 is actually equivalent to the condition $V_i = 1/n$, which means that the unit volume is equally partitioned by patches with different aspect ratios.

The function χ_1 can be expressed in simplified forms for some special cases. In the case of uniform ellipsoidal fluid patches, $\chi_1 = a_{20}^2v_1^{2/3}(\rho_{f_1}E_1 + \rho_{f_2}E_2(\phi_{10}/\phi_{20}))$. If the fluid patches are spheres, then $\chi_1 = a_{20}^2v_1^{2/3}(\rho_{f_1} + \rho_{f_2}(\phi_{10}/\phi_{20})(1 - (a_{10}/a_{20})))$. For nonuniform spherical patches, $\chi_1 = v_1^{2/3}(\rho_{f_1}\frac{1}{n}\sum_{i=1}^{n}a_{i20}^2 + \rho_{f_2}\frac{\phi_{10}}{\phi_{20}}\frac{1}{n}\sum_{i=1}^{n}a_{i20}^2(1 - \frac{a_{i10}}{a_{i20}}))$.

In equation A-20, we have assumed that the unit volume is equally partitioned by each aspect ratio, so that the equations

can be simplified, and the effects of the aspect ratio distribution on velocity are taken into consideration using only one parameter, i.e., the average aspect ratio. Changes in the distribution function of the aspect ratio will result in more complex equations and will be considered in a future work.

APPENDIX B

PLANE-WAVE ANALYSIS

According to Cardano's formula, the complex velocities can be written as

$$v_k=\frac{1}{\sqrt{Y}}=\frac{1}{\sqrt{z^k\left(-\frac{q}{2}+\sqrt{\frac{q^2}{4}+\frac{p^3}{27}}\right)^{1/3}+z^{2k}\left(-\frac{q}{2}-\sqrt{\frac{q^2}{4}+\frac{p^3}{27}}\right)^{1/3}}},$$
$$k=1,2,3, \tag{B-1}$$

where $p=(3AC-B^2)/(3A^2)$, $q=(2B^3-9ABC+27A^2D)/(27A^3)$, and $z=-(1/2)+(\sqrt{3}/2)i$.

The coefficients A, B, C, D are

$$A=a_{11}a_{22}a_{33}-a_{11}a_{23}a_{32}-a_{12}a_{21}a_{33}+a_{12}a_{23}a_{31}+a_{13}a_{21}a_{32}-a_{13}a_{22}a_{31}, \tag{B-2}$$

$$\begin{aligned}B=&a_{11}a_{22}b_{33}-a_{11}a_{23}b_{32}-a_{11}a_{32}b_{23}+a_{11}a_{33}b_{22}\\&-a_{12}a_{21}b_{33}+a_{12}a_{23}b_{31}\\&+a_{12}a_{31}b_{23}-a_{12}a_{33}b_{21}+a_{13}a_{21}b_{32}-a_{13}a_{22}b_{31}\\&-a_{13}a_{31}b_{22}+a_{13}a_{32}b_{21}\\&+a_{21}a_{32}b_{13}-a_{21}a_{33}b_{12}-a_{22}a_{31}b_{13}+a_{22}a_{33}b_{11}\\&+a_{23}a_{31}b_{12}-a_{23}a_{32}b_{11},\end{aligned} \tag{B-3}$$

$$\begin{aligned}C=&a_{11}b_{22}b_{33}-a_{11}b_{23}b_{32}-a_{12}b_{21}b_{33}+a_{12}b_{23}b_{31}\\&+a_{13}b_{21}b_{32}-a_{13}b_{22}b_{31}\\&-a_{21}b_{12}b_{33}+a_{21}b_{13}b_{32}+a_{22}b_{11}b_{33}-a_{22}b_{13}b_{31}\\&-a_{23}b_{11}b_{32}+a_{23}b_{12}b_{31}\\&+a_{31}b_{12}b_{23}-a_{31}b_{13}b_{22}-a_{32}b_{11}b_{23}+a_{32}b_{13}b_{21}\\&+a_{33}b_{11}b_{22}-a_{33}b_{12}b_{21},\end{aligned} \tag{B-4}$$

$$D=b_{11}b_{22}b_{33}-b_{11}b_{23}b_{32}-b_{12}b_{21}b_{33}+b_{12}b_{23}b_{31}+b_{13}b_{21}b_{32}-b_{13}b_{22}b_{31}. \tag{B-5}$$

The coefficients a_{ij}, b_{ij} are

$$a_{11}=A+2N+\frac{[Q_2\phi_1-Q_1\phi_2]^2}{S_1}, \tag{B-6}$$

$$a_{12}=a_{21}=Q_1-\frac{R_1\phi_2[Q_2\phi_1-Q_1\phi_2]}{S_1}, \tag{B-7}$$

$$a_{13}=a_{31}=Q_2+\frac{R_2\phi_1[Q_2\phi_1-Q_1\phi_2]}{S_1}, \tag{B-8}$$

$$a_{22}=R_1\left(1+\frac{R_1\phi_2^2}{S_1}\right), \tag{B-9}$$

$$a_{23}=a_{32}=-\frac{R_1R_2\phi_2\phi_1}{S_1}, \tag{B-10}$$

$$a_{33}=R_2+\frac{(R_2\phi_1)^2}{S_1}, \tag{B-11}$$

$$b_{11}=-\rho_{00}\omega^2+\iota\omega\sum_{m=1}^{2}b_m, \tag{B-12}$$

$$b_{12}=b_{21}=-\rho_{01}\omega^2-\iota\omega b_1, \tag{B-13}$$

$$b_{13}=b_{31}=-\rho_{02}\omega^2-\iota\omega b_2, \tag{B-14}$$

$$b_{22}=-\rho_{11}\omega^2+\iota\omega b_1, \tag{B-15}$$

$$b_{33}=-\rho_{22}\omega^2+\iota\omega b_2, \tag{B-16}$$

$$b_{23}=b_{32}=0, \tag{B-17}$$

$$S_1=\frac{1}{3}\phi_1\phi_2^2\omega(\iota\beta_1-\chi_1\omega)-(\phi_2^2R_1+\phi_1^2R_2). \tag{B-18}$$

REFERENCES

Aifantis, E. C., 1977, Introducing a multi-porous medium: Proceedings of the 15th Midwestern Mechanics Conference on Developments in Mechanics 8, 209–211.

Aifantis, E. C., 1979, A new interpretation of diffusion in high-diffusivity paths — A continuum approach: Acta Metallurgica, **27**, 683–691, doi: 10.1016/0001-6160(79)90019-1.

Aifantis, E. C., 1980, On the problem of diffusion in solids: Acta Mechanica, **37**, 265–296, doi: 10.1007/BF01202949.

Avseth, P. Å., 2000, Combining rock physics and sedimentology for seismic reservoir characterization of North Sea turbidite systems: Stanford University.

Ba, J., J. M. Carcione, O. Du, H. Zhao, and T. M. Müller, 2015, Seismic exploration of hydrocarbons in heterogeneous reservoirs, new theories, methods and applications: Elsevier Science.

Ba, J., J. M. Carcione, and J. X. Nie, 2011, Biot-Rayleigh theory of wave propagation in double-porosity media: Journal of Geophysical Research, **116**, B06202, doi: 10.1029/2010JB008185.

Ba, J., W. Xu, L. Fu, J. M. Carcione, and L. Zhang, 2017, Rock anelasticity due to patchy-saturation and fabric heterogeneity: A double double-porosity model of wave propagation: Journal of Geophysical Research: Solid Earth, **122** ,1949–1976, doi: 10.1002/2016JB013882.

Ba, J., J. Zhao, J. M. Carcione, and X. Huang, 2016, Compressional wave dispersion due to rock matrix stiffening by clay squirt flow: Geophysical Research Letters, **43**, 6186–6195, doi: 10.1002/2016GL069312.

Bacri, J.-C., and D. Salin, 1986, Sound velocity of a sandstone with oil and brine at different concentrations: Geophysical Research Letters, **13**, 326–328, doi: 10.1029/GL013i004p00326.

Barenblatt, G. I., I. P. Zheltov, and I. N. Kochina, 1960, Basic concepts in the theory of seepage of homogeneous liquids in fissured rocks [strata]: Journal of Applied Mathematics and Mechanics, **24**, 1286–1303, doi: 10.1016/0021-8928(60)90107-6.

Batzle, M. L., D. H. Han, and R. Hofmann, 2006, Fluid mobility and frequency-dependent seismic velocity — Direct measurements: Geophysics, **71**, no. 1, N1–N9, doi: 10.1190/1.2159053.

Berryman, J. G., and S. R. Pride, 2005, Dispersion of waves in porous cylinders with patchy saturation: Formulation and torsional waves: The Journal of the Acoustical Society of America, **117**, 1785–1795, doi: 10.1121/1.1861712.

Berryman, J. G., and H. F. Wang, 1995, The elastic coefficients of double-porosity models for fluid transport in jointed rock: Journal of Geophysical Research: Solid Earth, **100**, 24611–24627, doi: 10.1029/95JB02161.

Berryman, J. G., and H. F. Wang, 2000, Elastic wave propagation and attenuation in a double-porosity dual-permeability medium: International Journal of Rock Mechanics and Mining Sciences, **37**, 63–78, doi: 10.1016/S1365-1609(99)00092-1.

Boruah, N., and R. Chatterjee, 2010, Rock physics template (RPT) analysis of well logs and seismic data for lithology and fluid classification: Petroview, **3**, 13–27.

Buivol, V. N., 2006, Dynamics of ellipsoidal cavities in fluid: International Applied Mechanics, **42**, 145–151, doi: 10.1007/s10778-006-0069-0.

Cadoret, T., D. Marion, and B. Zinszner, 1995, Influence of frequency and fluid distribution on elastic wave velocities in partially saturated limestones: Journal of Geophysical Research: Solid Earth, **100**, 9789–9803, doi: 10.1029/95JB00757.

Cadoret, T., G. Mavko, and B. Zinszner, 1998, Fluid distribution effect on sonic attenuation in partially saturated limestones: Geophysics, **63**, 154–160, doi: 10.1190/1.1444308.

Dutta, N. C., and H. Odé, 1979a, Attenuation and dispersion of compressional waves in fluid-filled porous rocks with partial gas saturation (white model). 2. Results: Geophysics, **44**, 1789–1805, doi: 10.1190/1.1440939.

Dutta, N. C., and H. Odé, 1979b, Attenuation and dispersion of compressional waves in fluid-filled porous rocks with partial gas saturation (white model). 1. Biot theory: Geophysics, **44**, 1777–1788, doi: 10.1190/1.1440938.

Dutta, N. C., and A. J. Seriff, 1979, On White's model of attenuation in rocks with partial gas saturation: Geophysics, **44**, 1806–1812, doi: 10.1190/1.1440940.

Elsworth, D., and M. Bai, 1992, Flow-deformation response of dual-porosity media: Journal of Geotechnical Engineering, **118**, 107–124, doi: 10.1061/(ASCE)0733-9410(1992)118:1(107).

Gregory, A., 1976, Fluid saturation effects on dynamic elastic properties of sedimentary rocks: Geophysics, **41**, 895–921, doi: 10.1190/1.1440671.

Han, D.-H., H.-Z. Zhao, Q. Yao, and M. Batzle, 2007, Velocity of heavy oil sand: 77th Annual International Meeting, SEG, Expanded Abstracts, 1619–1623.

Helle, H. B., N. H. Pham, and J. M. Carcione, 2003, Velocity and attenuation in partially saturated rocks: Poroelastic numerical experiments: Geophysical Prospecting, **51**, 551–566, doi: 10.1046/j.1365-2478.2003.00393.x.

Johnson, D. L., 2001, Theory of frequency dependent acoustics in patchy-saturated porous media: Journal of the Acoustical Society of America, **110**, 682–694, doi: 10.1121/1.1381021.

Khaled, M. Y., D. E. Beskos, and E. C. Aifantis, 1984, On the theory of consolidation with double porosity — III. A finite element formulation: International Journal for Numerical and Analytical Methods in Geomechanics, **8**, 101–123, doi: 10.1002/(ISSN)1096-9853.

Knight, R., and R. Nolen-Hoeksema, 1990, A laboratory study of the dependence of elastic wave velocities on pore scale fluid distribution: Geophysical Research Letters, **17**, 1529–1532, doi: 10.1029/GL017i010p01529.

Lebedev, M., J. Toms-Stewart, B. Clennell, M. Pervukhina, V. Shulakova, L. Paterson, B. Gurevich, and F. Wenzlau, 2009, Direct laboratory observation of patchy saturation and its effects on ultrasonic velocities: The Leading Edge, **28**, 24–27, doi: 10.1190/1.3064142.

Liu, J., T. M. Müller, Q. Qi, M. Lebedev, and W. Sun, 2016, Velocity-saturation relation in partially saturated rocks: Modelling the effect of injection rate changes: Geophysical Prospecting, **64**, 1054–1066, doi: 10.1111/1365-2478.12376.

Lopes, S., and M. Lebedev, 2012, Research note: Laboratory study of the influence of changing the injection rate on the geometry of the fluid front and on P-wave ultrasonic velocities in sandstone: Geophysical Prospecting, **60**, 572–580, doi: 10.1111/j.1365-2478.2011.01009.x.

Lopes, S., M. Lebedev, T. M. Müller, M. B. Clennell, and B. Gurevich, 2014, Forced imbibition into a limestone: Measuring P-wave velocity and water saturation dependence on injection rate: Geophysical Prospecting, **62**, 1126–1142, doi: 10.1111/1365-2478.12111.

Mavko, G., and T. Mukerji, 1998, Bounds on low-frequency seismic velocities in partially saturated rocks: Geophysics, **63**, 918–924, doi: 10.1190/1.1444402.

Müller, T., and B. Gurevich, 2004, One-dimensional random patchy saturation model for velocity and attenuation in porous rocks: Geophysics, **69**, 1166–1172, doi: 10.1190/1.1801934.

Müller, T., B. Gurevich, and M. Lebedev, 2010, Seismic wave attenuation and dispersion resulting from wave-induced flow in porous rocks — A review: Geophysics, **75**, no. 5, 75A147–75A164, doi: 10.1190/1.3463417.

Müller, T. M., J. Toms-Stewart, and F. Wenzlau, 2008, Velocity-saturation relation for partially saturated rocks with fractal pore fluid distribution: Geophysical Research Letters, **35**, L09306, doi: 10.1029/2007GL033074.

Murphy, W. F., 1984, Acoustic measures of partial gas saturation in tight sandstones: Journal of Geophysical Research, **89**, 11549–11559, doi: 10.1029/JB089iB13p11549.

Pride, S. R., J. G. Berryman, and J. M. Harris, 2004, Seismic attenuation due to wave-induced flow: Journal of Geophysical Research, **109**, B01201, doi: 10.1029/2003JB002639.

Quintal, B., H. Steeb, M. Frehner, and S. M. Schmalholz, 2011, Quasi-static finite element modeling of seismic attenuation and dispersion due to wave-induced fluid flow in poroelastic media: Journal of Geophysical Research: Solid Earth, **116**, B01201, doi: 10.1029/2010JB007475.

Rubino, J. G., and K. Holliger, 2012, Seismic attenuation and velocity dispersion in heterogeneous partially saturated porous rocks: Geophysical Journal International, **188**, 1088–1102, doi: 10.1111/j.1365-246X.2011.05291.x.

Sharma, M. D., 2017, Wave propagation in double-porosity dual-permeability materials: Velocity and attenuation: Advances in Water Resources, **106**, 132–143, doi: 10.1016/j.advwatres.2017.02.016.

Sun, W., J. Ba, and J. E. M. Carcione, 2016, Theory of wave propagation in partially saturated double-porosity rocks: A triple-layer patchy model: Geophysical Journal International, **205**, 22–37, doi: 10.1093/gji/ggv551.

Sun, W., J. Ba, T. M. Müller, J. M. Carcione, and H. Cao, 2015, Comparison of P-wave attenuation models of wave-induced flow: Geophysical Prospecting, **63**, 378–390, doi: 10.1111/1365-2478.12196.

Toms, J., T. M. Müller, R. Ciz, and B. Gurevich, 2006, Comparative review of theoretical models for elastic wave attenuation and dispersion in partially saturated rocks: Soil Dynamics and Earthquake Engineering, **26**, 548–565, doi: 10.1016/j.soildyn.2006.01.008.

Toms, J., T. M. Müller, and B. Gurevich, 2007, Seismic attenuation in porous rocks with random patchy saturation: Geophysical Prospecting, **55**, 671–678, doi: 10.1111/j.1365-2478.2007.00644.x.

Toms-Stewart, J., T. Müller, B. Gurevich, and L. Paterson, 2009, Statistical characterization of gas-patch distributions in partially saturated rocks: Geophysics, **74**, no. 2, WA51–WA64, doi: 10.1190/1.3073007.

Tserkovnyak, Y., and D. L. Johnson, 2002, Can one hear the shape of a saturation patch? : Geophysical Research Letters, **29**, 1108, doi: 10.1029/2001GL014709.

White, J. E., 1975, Computed seismic speeds and attenuation in rocks with partial gas saturation: Geophysics, **40**, 224–232, doi doi: 10.1190/1.1440520.

White, J. E., N. G. Mikhaylova, and F. M. Lyakhovitskiy, 1975, Low-frequency seismic waves in fluid-saturated layered rocks: The Journal of the Acoustical Society of America, **57**, 654–659.

Wilson, R. K., and E. C. Aifantis, 1982, On the theory of consolidation with double porosity: International Journal of Engineering Science, **20**, 1009–1035, doi: 10.1016/0020-7225(82)90036-2.

Wyllie, M., A. Gregory, and L. Gardner, 1956, Elastic wave velocities in heterogeneous and porous media: Geophysics, **21**, 41–70, doi: 10.1190/1.1438217.

Wyllie, M., A. Gregory, and G. Gardner, 1958, An experimental investigation of factors affecting elastic wave velocities in porous media: Geophysics, **23**, 459–493, doi: 10.1190/1.1438493.

Zheng, P., B. Ding, and X. Sun, 2017, Elastic wave attenuation and dispersion induced by mesoscopic flow in double-porosity rocks: International Journal of Rock Mechanics and Mining Sciences, **91**, 104–111, doi: 10.1016/j.ijrmms.2016.11.018.